Electronics Letters, Volume 53, Issue 15, 20 July 2017, p. 991 – 995. DOI: 10.1049/el.2017.1570

# Through-Wall Detection and Imaging of a Vibrating Target Using Synthetic Aperture Radar

B. Corbett, D. Andre and M. Finnis

This paper explains the development of a through-wall synthetic aperture radar (SAR) simulator, which is being used to investigate the SAR artefacts originating from vibrating target's, known as paired echoes. The simulation and experimental results both show that paired echoes can be detected and imaged through a wall, with a noticeable reduction in intensity, resulting in the number of visible echoes to be reduced in brightness and appear shifted in location in a through-wall SAR image.

*Introduction:* One of the key desirable outcomes of the Remote Intelligence of Building Interiors (RIBI) programme is in the detection of objects and activities within closed buildings, underground bunkers etc. The activities of interest may involve the use of running machinery, therefore being able to accurately detect this will fundamentally aid in the RIBI programme overall goal.

Low frequency synthetic aperture radar (SAR) can provide one such solution. It has been shown that SAR can be used to generate images through a variety of mediums, with varying degrees of accuracy and clarity [1, 2].

The detection and imaging of a vibrating scatterer is the focal point of this investigation. This is because an object following this kind of motion, for example an object moving with its displacement in the form of, for example, a sinusoid wave, can be used as a representation for a variety of real world objects. For example this could represent aspects of a running machine, i.e. a generator, fan, etc. Therefore understanding the effects produced within a SAR image from a vibrating object behind a wall, could lead to the capability of being able to identify and recognise running machinery within a building from a stand-off location.

It is well known that a vibrating target within the SAR imaged scene will theoretically produce paired echoes, artefacts which are seen either side of the true target position in a SAR image [3, 4, 5]. How these paired echoes appear when imaged through a wall, when various types of vibration are considered and when different radar geometries are used, is therefore the focal point of the research described.

*Initial SAR Signal Model Simulation:* The initial SAR signal model developed follows a stop/start approximation (therefore representing the Cranfield University GBSAR laboratory set-up [21]), which assumes static (non-vibrating) stationary point scatterers located within a vacuum. The backprojection algorithm is used for the image processing of both simulation and measurement data [6]. The signal model has been developed for both a monostatic (the radar transmit and recieve antennas share the same location) and bistatic radar geometries (the transmit and receive antennas are positioned at two independent locations during each measurement [7]).

*Target Vibration Signal Model:* The theoretical effects of how a vibrating target will appear within a SAR image have been detailed previously [3, 4, 5]. A vibrating scatterer's location can be represented by applying a continuous oscillating displacement to the scatterer's location in the range dimension, as a function of time. Equation (1) represents this motion as a sinusoidal vibration, where $\omega_{vib}$ is the angular frequency of the target's vibration, $\omega_{vib} = 2\pi f_{vib}$, $f_{vib}$ being the frequency of the target's vibration (it is assumed that the period of oscillation is much lower than the radar chirp pulse duration), $t$ is the slow-time position of the scan, hence this function relates to the time reference the radar antenna horns move in [4]. Finally, $y_0$ is the original location of the scatterer within space, and $A_{vib}$ is the amplitude of the vibration.

$$y_{vib} = y_0 + A_{vib} \cdot \sin\left(\omega_{vib} t\right) \tag{1}$$

The value inputted for $t$ (slow time), can be given as a factor of radar aperture distance travelled ($A_p$), therefore $y_{vib}$ and $Ap$ become functions of the azimuthal sample number ($N_x$).

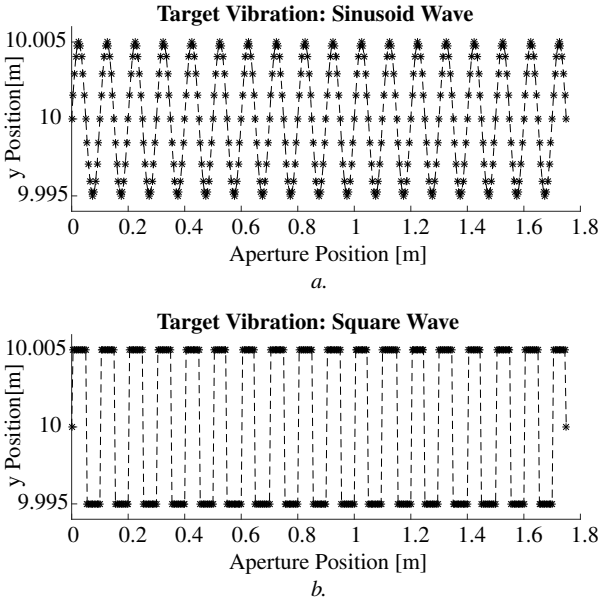


**Fig. 1** *Example vibrational outputs from equations (2) and (3).*
*a. Sinusoid vibration.*
*b. Square wave vibration.*

$$y_{vib}(N_x) = y_0 + A_{vib} \cdot \sin\left(\omega_{vib} \frac{Ap\,(N_x)}{2}\right) \tag{2}$$

An *extreme* form of vibration considered for comparison, is one that follows a square wave, see equation (3) [8].

$$y_{vib}(N_x) = y_0 + A_{vib} \cdot \text{signum}\left(\sin\left(\omega_{vib} \frac{Ap\,(N_x)}{2}\right)\right) \tag{3}$$

Fig. 1 shows the outputs produced from equations (2) and (3), where the vibrations are applied to a target located at $10\,[m]$ in range. Both vibrations have a $10\,[Hz]$ frequency and an amplitude of $\pm 5\,[mm]$, with an effective constant antenna velocity of $2.06\,\left[\frac{m}{s}\right]$. The dotted line represents the theoretical motion of the vibration, if the antennas were moving continuously. While the asterisks show the target's position at each of the radar measurement positions, following a stop/start approximation.

A practical implementation of both sinusoid and square vibrations are shown in Fig. 1. Implementing both of the vibrations to two individual point scatterers used within the simulation model developed, gives rise to results consistent with the theoretical analysis by [3, 4, 5], such that sets of paired echoes appear either side of the scatterers true position [5], as shown in Fig. 2.

The radar parameters for simulation are as follows: Centre frequency: $5.5\,[GHz]$, Bandwidth: $2\,[GHz]$, Aperture: $3.5\,[m]$, Height: $2.79\,[m]$, Azimuth samples $351$ and Frequency samples $801$. The radar antennas are located at $-10\,[m]$ down range, therefore are located beyond the top of the image shown (this is the case for all simulation and measurement SAR images throughout this piece of work). One scatterer is located at $[0, 1]\,[m]$ and has a square wave vibration and the second is located at $[0, -1]\,[m]$ and has a sinusoidal vibration, where the coordinate system is as follows [cross-range, range] $[m]$. Both scatterers have a vibrational frequency of $10\,[Hz]$ and a vibrational amplitude of $5\,[mm]$, with an effective constant antenna velocity of $2.06\,\left[\frac{m}{s}\right]$.

*Electromagnetic Wave Propagation:* To develop an accurate signal model for the simulation of through-wall SAR imagery, the effects upon an electromagnetic wave as it propagates through a medium need to be considered. The first of these effects implemented into the simulation model is the attenuation of a wave.

If an electromagnetic wave passes through a medium whose conductivity, $\sigma > 0$, it will experience energy losses to both its electric and magnetic fields, hence resulting in the overall attenuation of the electromagnetic wave, therefore producing an overall power loss in the electromagnetic wave as energy is transferred from the wave to the medium [9]. Boundary reflection and transmission coefficient losses are not being considered.

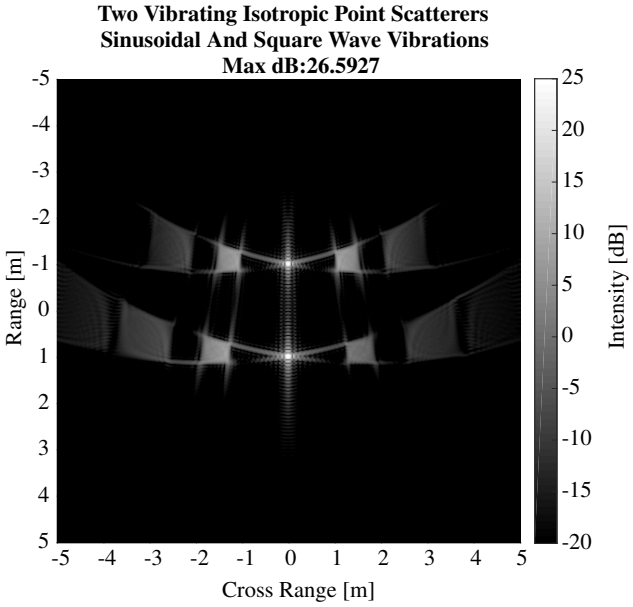


**Fig. 2** *SAR image of two vibrating isotropic points scatterers in a vacuum. One scatterer is located at* $[0, 1]$ $[m]$ *and has a square wave vibration and the second is located at* $[0, -1]$ $[m]$ *and has a sinusoidal vibration.*

General building materials, i.e. what will be considered for this piece of work; e.g. concrete can be considered as a lossy dielectric material, hence a partially conducting material. Therefore the material is both an imperfect dielectric and imperfect conductor [10]. For lossy dielectric materials, it is therefore assumed that both conduction and dielectric effects in the material influence the absorption of the transmitted electromagnetic waves, hence causing the wave to attenuate [11].

The dielectric constant for a material, also known as the absolute permittivity is represented $\epsilon = \epsilon_r \epsilon_0$, and the absolute permeability of a material is as follows, $\mu = \mu_r \mu_0$, [10, 11, 12].

Here $\epsilon_0$ represents the absolute electric permittivity of free space, also known as the electric constant $(8 \times 10^{-12} \left[\frac{F}{m}\right])$. $\epsilon_r$ is the relative permittivity of the medium. $\mu_0$ is the absolute permeability of free space $(4\pi^{-7} \left[\frac{N}{A^2}\right])$, $\mu_r$ is the relative permeability and is approximately equal to 1 [10, 11, 12].

When modelling the effects of an attenuating wave, through a lossy medium it is useful to define a complex value both the relative permittivity $(\epsilon_r)$ and the conductivity of the medium being modelled [11], see equations (4) and (5), where $x'$ and $x''$ are the real and complex terms respectively [10, 11].

$$\epsilon_r = \epsilon_r' - i\epsilon_r'' \tag{4}$$

$$\sigma = \sigma' - i\sigma'' \tag{5}$$

From equation (4) and using Maxwell's equations, one can obtain equation (6), which links both the (real) conductivity $(\sigma')$ of the material (from equation (5)) and the angular frequency $(\omega)$ of the electromagnetic wave to the permittivity of the medium $(\epsilon_r)$ [11, 12, 13].

$$\epsilon_r = \epsilon_r' - i\frac{\sigma'}{\epsilon_0 \omega} \tag{6}$$

The effects of attenuation upon an electromagnetic wave travelling through a lossy medium can also be derived from Maxwell's equations resulting in a new equation for wave number $(\hat{k})$, for an attenuating wave, equations (7) to (9), as follows. [9, 13, 14].

$$\hat{k} = \alpha + i\beta \tag{7}$$

*Where:*

$$\alpha = \omega \sqrt{\frac{\mu\epsilon}{2}\left[\sqrt{1 + \left[\frac{\sigma'}{\omega\epsilon}\right]^2} - 1\right]} \tag{8}$$

$$\beta = \omega \sqrt{\frac{\mu\epsilon}{2}\left[\sqrt{1 + \left[\frac{\sigma'}{\omega\epsilon}\right]^2} + 1\right]} \tag{9}$$

In equations, (8) and (9), $\alpha$ represents the attenuation effects upon the wave and $\beta$ represents the phase constant of the wave.

*Electromagnetic Wave Refraction:* To form a focused SAR image (from a signal processing perspective) of a target within or beyond another medium, one needs to calculate the distance the electromagnetic wave has travelled, as it propagates though multiple mediums. Considering only a two medium scenario, the path distance travelled can be calculated using an approximation method presented in [15]. [15] assumes that one knows the location of the electromagnetic waves source, the target's location and the location of the planar boundary separating the two mediums. It is also assumed that the absolute permittivity of the medium the target is located in, is equal to or greater than, the absolute permittivity of the medium the antenna is located in. When considering multiple layers however the final assumption cannot be made [15, 16]. As [15] is only an approximation method, it is therefore designed to be computationally efficient, however, if accuracy is required, then [17] presents a double quadratic equation, that can be solved symbolically, to find the refraction point for a path of light travelling between two mediums.

Expanding on these solutions and moving to multiple mediums, [15] describes a time minimisation approach, where their algorithm changes the location of the points of refraction until the travel time of the ray is minimised to within a level of tolerance [15]. Another approach is to form a set of transcendental equations to be solved numerically to find an accurate solution for each of the angles of incidence and refraction at each of the planar boundaries separating the mediums and then the locations of the points of refraction can be determined from this. As explained in [16, 18], these methods are computationally expensive.

There have been developments in efficiency that have built upon the fundamental approaches of either time minimisation, or a numerical solution to a set of transcendental equations. Hence the approach taken in [18], where the authors have simplified a three medium scenario, and have made the assumption that it can be solved as a two medium problem by moving the range location of the antenna to the range position of the first planar boundary of mediums one and two. Therefore, only the location of one refraction point needs to be calculated at the planar boundary of medium two and three.

However, [16] identified the approaches mentioned previously could be improved upon and formulated an approach to solve the problem of calculating the refraction point locations, efficiently, numerically and from a geometrical perspective. As part of this project, following the methodology of [16], the mathematics has been re-evaluated and a new version of their two dimensional algorithm has been developed and further expanded to three-dimensions for any number of mediums. The developed algorithm and associated documentation can be found here [22].

*Through-Wall Signal Model Implementation into the Initial SAR Model:* From the original signal model for a monostatic SAR geometry [6]. The final stage in the model is to generate the phase history $(P_h)$ of the received signal pulses. This can be completed using equation (10). Where $f_l$ is the $l^{th}$ frequency, and $r_m$ is the $m^{th}$ total distance travelled by the emitted electromagnetic wave, this represents the two-way distance travelled by the wave.

$$P_h\left(k_l, r_m\right) = e^{-i(k_l r_m)} \tag{10}$$

*Where:*

$$k_l = \frac{2\pi f_l}{c} \tag{11}$$

The next part of the phase history calculation is to correct for the location of the imaged scene centre. In [5] it is explained that the use of a differential range can be used within equation (10), therefore, $r_m$ is now calculated to be the differential range. The differential range is the difference between the range to and from the antenna and target and the range to and from the antenna and scene centre.

For the case where there are attenuation effects, (10) is reformulated to produce the the corrected phase history $(P_{hc})$ for the developed SAR signal model for through-wall simulations. Where $m_t$ is the total number of mediums the electromagnetic wave propagates through, therefore $m$ represents the index of medium in consideration. $\hat{k}_m$ is therefore the wave number for each of the mediums, $R_m$ is the distance travelled by the wave through each individual mediums and $R_{sc}$ is the distance from the antenna to the imaging scene centre. Both $R_m$ and $R_sc$ represent the two-way distances travelled by the electromagnetic wave.

$$P_{hc} = e^{-i\left(\sum_{m=1}^{m_t} \hat{k}_m R_m\right)} \cdot e^{-i(kR_{sc})} \tag{12}$$

An example of this through-wall simulation is shown Fig. 3 and Fig. 4. Two vibrating isotropic point scatterers are located before and after a single medium. The areas before and after the medium are considered to be a vacuum. The medium itself is considered to be of infinite extent in the cross range dimensions and runs from $0.05\,[m]$ to $-0.05\,[m]$ in the range dimension, and is representing a concrete material, which has a (real) relative permittivity of 7 and a conductivity of $1 \times 10^{-1.25}\,\left[\frac{S}{m}\right]$ [10].

The sinusoidal vibration applied to both of the scatterers in Fig. 3 have the same frequency, amplitude and location of the vibrating scatterers shown in Fig. 2 ($10\,[Hz]$ and $5\,[mm]$ respectively, with an effective antenna velocity of $2.06\,\left[\frac{m}{s}\right]$).

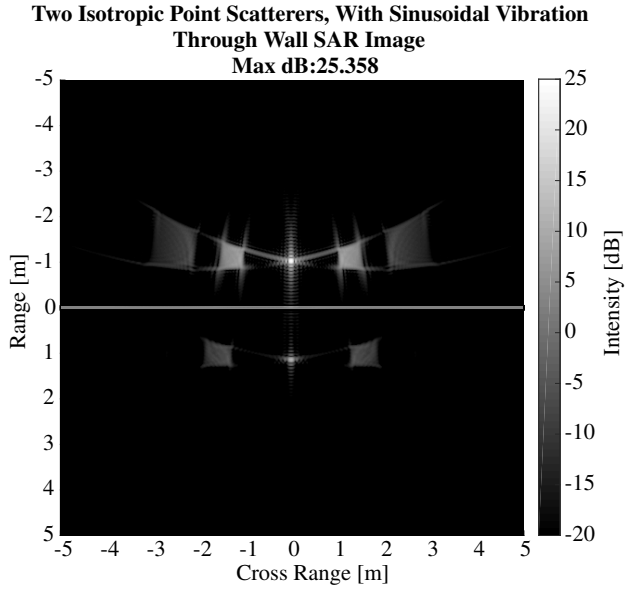


**Fig. 3** *Monostatic SAR simulation of two vibrating isotropic point scatterers located before and after a single concrete medium, highlighted by the white rectangle (this is not part of the SAR image).*

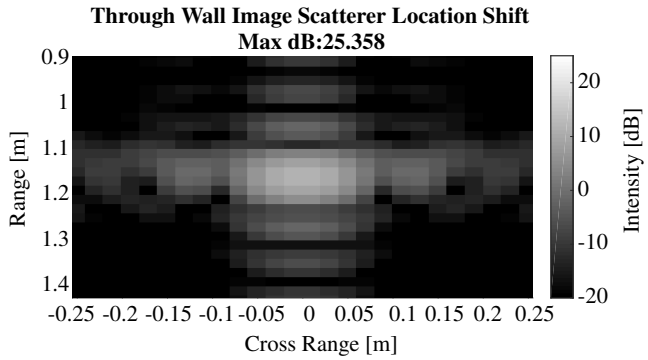


**Fig. 4** *Zoomed in region of Fig. 3, highlighting the artificial location shift down range, for the scatterer located behind the wall. This can be seen to be* $\approx 0.15\,[m]$*, from its actual location of* $[0, 1]\,[m]$.

However, for the scatterer located behind the wall the second repeated occurrence of the paired echoes visible in Fig. 2 can no longer be seen in Fig. 3 because the signature brightness has fallen below the set intensity dynamic range limit. Secondly in Fig. 4 the scatterer located behind the wall also appears to have shifted location in range, increasing its imaged location away from the antennas, by $\approx 0.15\,[m]$ due to the effects of electromagnetic wave refraction. This happens due to the decrease in the velocity of the electromagnetic wave as it propagates through the wall, causing it to refract. Fig. 2 and Fig. 3 are relatively calibrated to each other (but not absolutely calibrated) so that this comparison can be made.

*Experimental Results:* To validate the signal models developed during the simulation phase, measurements were performed with the Cranfield University GBSAR system [21]. To replicate the vibrational effects shown in simulated SAR images, a moving target was developed, that could move small distances accurately and communicate with the radar scanner so that the two remained in synchronization with each other as measurements were taken as the antennas traverse across the SAR aperture. Because of it's flexible and fast prototyping properties and with the ability of being controlled over Bluetooth through MATLAB, the Lego Mindstorms System [19, 20] was selected for the development of the programmable moving target platform.

Fig. 5 shows the through-wall scenario experimental set up. The wall is set up so that it ensures there is still no line-of-sight to the radar antennas at any position across the SAR aperture, from the perspective of the trihedral on the moving rover. Table 1 lists the radar set-up parameters used throughout all the measurements.


**Fig. 5** *Experimental measurement scene set up. The* $876 \times 645\,[mm]$ *breeze block wall is situated* $10\,[m]$ *down range from the radar antenna horns, on the SAR scanner. The vibration rover with situated trihedral is located* $1\,[m]$ *behind the wall.*

**Table 1:** Experimental Measurement Parameters

| Parameter | Value |
|---|---|
| Aperture $[m]$ | 3.5 |
| Azimuthal Samples | 351 |
| Centre Frequency $[GHz]$ | 5.5 |
| Bandwidth $[GHz]$ | 2 |
| Frequency Samples | 801 |
| Antenna Altitude $[m]$ | 2.79 |
| Range to Scene Centre & Wall $[m]$ | 10 |
| Range to Target $[m]$ | 11 |
| Wall Material | Standard concrete masonry unit. Predicted coefficients: 1. $\epsilon_r = 7$ 2. $\sigma = 1 \times 10^{-1.25}\,\left[\frac{S}{m}\right]$ |
| Wall Height $[mm]$ | 645 |
| Wall Width $[mm]$ | 876 |
| Wall Thickness $[mm]$ | 97 |
| Target | Trihedral |
| Target Size $[mm]$ | $250 \times 250 \times 250$ |

The two most notable results are shown in Fig. 6 and Fig. 7, which were obtained for a monostatic radar geometry, with the same vibration parameters as used within simulation, therefore a $5\,[mm]$ amplitude and $10\,[Hz]$ frequency, with an effective velocity of $2.06\,\left[\frac{m}{s}\right]$ . All measurement SAR images (Fig. 6 and Fig. 7) are relatively calibrated to each other (but not absolutely calibrated).

The same effects shown in the SAR image simulation results (Fig. 3 and Fig. 4) can be seen in the measurement images, this firstly being the reduction in the intensity of the imaged target behind the wall due to attenuation and therefore the reduction in the number of paired echoes visible in the image, as they now fall below the set intensity dynamic range limit of the images. Secondly, highlighted by Fig. 8 is the artificial range shift of the target within the image, by $\approx 0.18\,[m]$, a result similar to that shown in Fig. 4. This is very promising as a validation result for the simulation developed.

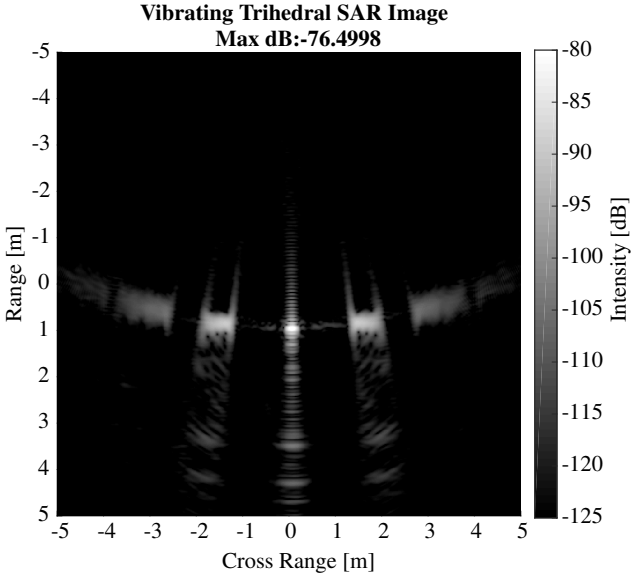


**Fig. 6** *SAR image of a trihedral target following a sinusoidal motion, measured without obstruction. The vibration has a* $5\,[mm]$ *amplitude and* $10\,[Hz]$ *frequency, therefore emulating a* $1.7\,[sec]$ *flight time, if the antennas were moving with a constant velocity across the* $3.5\,[m]$ *aperture.*

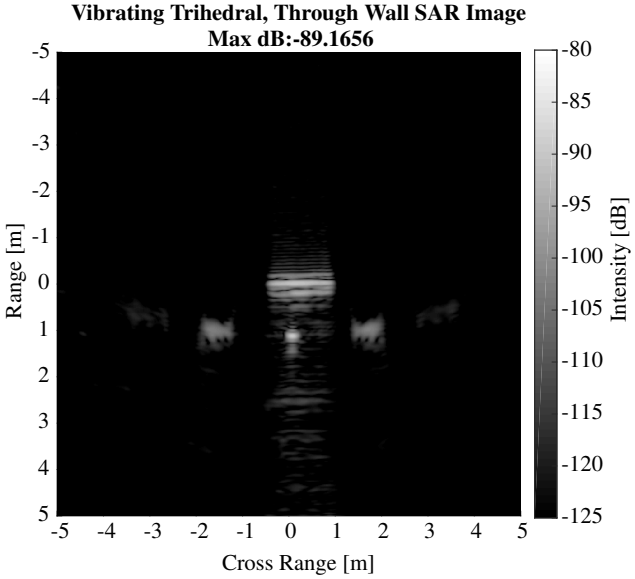


**Fig. 7** *Measurement SAR image of a trihedral located behind the breezeblock wall (as shown in Fig. 5) following a sinusoidal motion.*

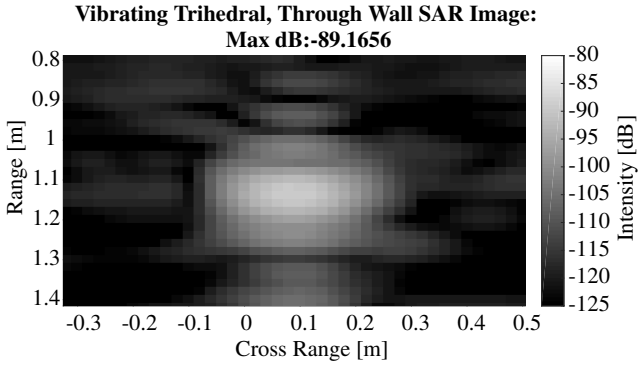


**Fig. 8** *Zoomed in region of Fig. 7, highlighting the artificial location shift down range. This can be seen to be* $\approx 0.18\,[m]$*, from its actual location of* $[0, 1]\,[m]$.

*Conclusion:* A prediction capability for modeling SAR collections of vibrating scatterers with and without intervening walls was developed. The results of the predictions were successfully validated against laboratory measurements conducted with the Cranfield University GBSAR system. Since this work has been completed, a data set for a bi-static radar geometry with the same target vibration and wall parameters has been collected. The preliminary results from this data set are again promising, with paired echoes produced by a target's vibration being successfully detected and imaged through a wall.

*Acknowledgment:* This work was funded by DSTL under the RIBI programme.

B. Corbett and D. Andre (*Centre for Electronic Warfare, Information and Cyber (EWIC), Cranfield University, UK Defence Academy, UK*)

M. Finnis (*Centre For Defence Engineering, Cranfield University, UK Defence Academy, UK*)

Email: b.corbett@cranfield.ac.uk

## References

1 Seng, C,H.: 'Image processing for enhanced through-the-wall radar imaging', *University of Wollongong*, 2013

2 Amin, M, Ahmad, F.: 'Through-the-Wall Radar Imaging: Theory and Applications', *Research Gate*, 2014

3 Ruegg, M, Meier, E, and Nuesch, D.: 'Constant motion, acceleration, vibration, and rotation of objects in SAR data'. *Remote Sensing. International Society for Optics and Photonics*, 2005

4 Sullivan, RJ.: 'Microwave Radar Imaging and Advanced Concepts', 2000, pp. 219-221

5 Carrara, W. and Goodman, R.: 'RMM. Spotlight Synthetic Aperture Radar Signal Processing Algorithms', *Artech House*, 1995

6 Gorham, L and Moore, L.: 'SAR image formation toolbox for MATLAB', *SPIE Defense, Security, and Sensing. International Society for Optics and Photonics*, 2010

7 Barnes, C.: 'Synthetic Aperture Radar - Wave Theory Foundations - Analysis and Algorithms', 2014, pp. 22

8 Weisstein, E.:. 'Square Wave. Mathworld-A Wolfram Web Resource', *URL: http://mathworld.wolfram.com/ SquareWave.html.*, 2017

9 Sadiku, M.: 'Elements of Electromagnetics', *Sixth Edition. Oxford University Press*, 2014, pp.410-472

10 Daniels, D.: 'Ground Penetrating Radar', *2nd. Edition IET*, 2004

11 ITU-R.: 'Effects of building materials and structures on radiowave propagation above about 100 MHz', *Technical Report. International Telecommunication Union, Radio Communication Sector*, 2015

12 Lei, T.: 'Optics. Lecture Series. Physics 4510', *URL: http://www.colorado.edu/physics/phys4510/phys4510_fa05/*, 2014

13 Balanis, C.: 'Advanced Engineering Electromagnetics'. *John Wiley & Sons*, 1989

14 Morrow, I and Van Genderen, P.: 'A polarimetric near-field backpropagation algorithm for application to GPR imaging of mines and minelike objects', *Proceedings of SPIE, the International Society for Optical Engineering*, 2001

15 Johansson, E and Mast, J.: 'Three-dimensional ground- penetrating radar imaging using synthetic aperture time-domain focusing', *SPIE's 1994 International Symposium on Optics, Imaging, and Instrumentation. International Society for Optics and Photonics*, 1994, pp. 205-214

16 Wang, G, Wu, R, and Zhang, M.: 'Quick determination of refraction points for GPR SAR imaging', *Defense and Security. International Society for Optics and Photonics*, 2005, pp. 544-548

17 Dziewierz, J and Gachagan, A.: 'Correspondence: Computationally efficient solution of snell's law of refraction', *IEEE transactions on ultrasonics, ferroelectrics, and frequency control*, 2013, pp. 60:1256-1259

18 Jin, T, Chen, B, and Zhou, Z.: 'Image-domain estimation of wall parameters for autofocusing of through-the-wall SAR imagery', *IEEE Transactions on Geoscience and Remote Sensing*, 2013, pp. 51:1836-1843

19 Lego: 'Mindstorms - EV3', *URL: https://www.lego.com/en-gb/mindstorms*, 2017

20 Kopcazka, M, Schneider, D, Staas, M.: 'RWTH - Mindstorms NXT Toolbox for MATLAB', *http://www.mindstorms.rwth-aachen.de/trac/*, 2016

21 Andre, D, Morrison, K.: 'Very High Resolution Coherent Change Detection ', *IEEE*, 2015

22 Corbett, B.: 'Electromagnetic Wave Path Finding Algorithm, Applied to Synthetic Aperture Radar', *Cranfield CORD*, DOI: 10.17862/cranfield.rd.4903448, 2017